POLITECNICO DI TORINO
Repository ISTITUZIONALE

Mastering Lateral Radiation Losses in Tunable VCSELs

(Article begins on next page)

19 April 2024

Mastering Lateral Radiation Losses
in Tunable VCSELs

Pierluigi Debernardi, Alberto Tibaldi, and Renato Orta, *Senior Member, IEEE*

Abstract—This work deals with tunable vertical-cavity surface-emitting lasers (VCSELs). The strong increase of the threshold gain at the tuning range edges motivates the investigation of the degradation mechanisms presented in this paper. A campaign of simulations performed with our in-house Vcsel ELectroMagnetic (VELM) simulation code, combined with a novel approach based on the study of the Poynting vector, allowed to identify significant lateral radiation losses. The proposal of technology-affordable countermeasures rests of the proper understanding of these phenomena.

Index Terms—Tunable VCSELs, scattering losses, lateral radiation losses, diffraction.

I. Introduction

THE introduction of tunable vertical-cavity surface-emitting lasers (VCSELs) in mass market applications could start a revolution in several branches of engineering [1]. Remarkable examples are the integrated monolithic MEMS-tunable VCSEL around 850 nm [2], [3], and the record 102 nm continuous single-mode tuning range VCSEL realized in the SUBTUNE EU project in the 1.55 μm window [4]. Tunable VCSELs are also key components in biomedical diagnostics [5], such as optical coherence tomography instruments working around 1.05 μm [6]-[7], and 1.31 μm [8].

Another application concerns the detection of chemical species, for instance for air quality monitoring. This is performed by means of the spectroscopic investigation of their strong absorption peaks in the mid-infrared (mid-IR) window. This range can be covered by antimonide [9], [10] or, as in this work, by lead chalcogenide semiconductors [11]. A possible implementation of a tunable laser consists of a movable mirror, which can be either a distributed Bragg reflector (DBR) or a high-contrast grating (HCG) [12], and a fixed half-VCSEL including the active region and the emitting section. Tuning is achieved by changing the air-gap between the top and bottom parts.

This paper describes the results of a campaign of simulations performed by means of our in-house 3-D vectorial simulator Vcsel ELectroMagnetic (VELM) [13], [14]. These simulations revealed unexpected peaks of the threshold gain at the tuning edges, which might prevent lasing operation. These can be attributed to phenomena already described in the
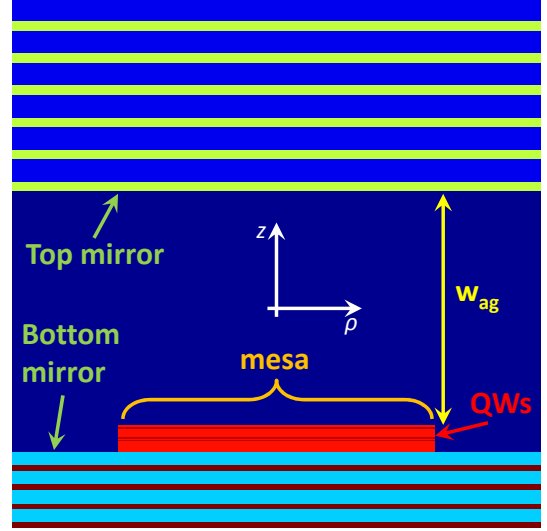
P. Debernardi and A. Tibaldi are with the Consiglio Nazionale delle Ricerche (CNR), Istituto di Elettronica e di Ingegneria dell'Informazione e delle Telecomunicazioni (IEIIT), 10129 Turin, Italy, e-mail: alberto.tibaldi@ieiit.cnr.it.

R. Orta is with the Department of Electronics and Telecommunications, Politecnico di Torino, Torino, 10129 Italy, and with CNR-IEIIT.

Fig. 1. Sketch of the bottom-emitting tunable VCSEL where the relevant sections are indicated: the mesa, the air-gap w_{ag}, the QWs, the top and bottom (output) mirrors. The color map indicates refractive index values from low (blue) to high (red).

literature for masers, gas lasers and even VCSELs by means of simplified cavity models and classified with the generic keyword *scattering losses* [15]-[16]. In this work VELM has been complemented by a Poynting vector analysis tool, which allows to relate these threshold peaks to the radiation of optical power towards the lateral directions. Deeper insight into this mechanism is achieved by relating the VELM simulation results to simplified 1-D analyses. Various solutions to reduce such losses are proposed in the paper.

II. Performance degradation in tunable VCSELs

The bottom-emitting VCSEL under investigation is described in [11] and sketched in Fig. 1. The top DBR is a stack of Si/SiO$_2$ layers. The DBR implementing the bottom mirror consists of $\lambda/4$ EuTe/Pb$_x$Eu$_{1-x}$Te pairs grown on Si ($n = 2.4/5.31$). The Pb$_y$Sr$_{1-y}$Se 1-λ cavity containing the active material lies above such mirror. The mesa structure (about 30 μm diameter), obtained by etching the material deposited on the bottom DBR, is introduced to counteract the temperature-induced antiguiding effect typical of lead chalcogenides [11]; except for that, the geometry is flat. If not differently specified, all dielectric layers are assumed to be lossless.

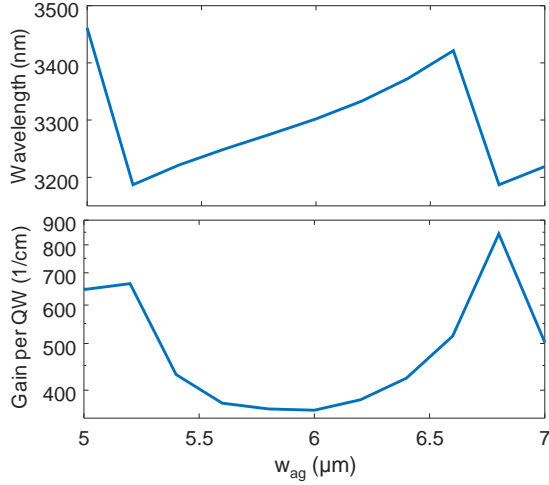The tuning features are simulated with VELM [4], [17], which solves Maxwell's equations in cylindrical coordinates.

Fig. 2. Tuning features of the VCSEL of Fig. 1: emission wavelength (top) and threshold gain per QW (bottom) versus air-gap width w_{ag}.

Fig. 4. Longitudinal power flux $P_z(z)$ computed according to (1). The solid blue and red lines refer to 3-D simulations with $w_{\mathrm{ag}} = 6\,\mu\mathrm{m}$ ($G_{\mathrm{th}} \simeq 350/\mathrm{cm}$) and $w_{\mathrm{ag}} = 6.8\,\mu\mathrm{m}$ ($G_{\mathrm{th}} \simeq 800/\mathrm{cm}$). The dashed magenta and black lines (almost coincident) are the corresponding 1-D simulations. The contributions of top and bottom DBRs and lateral radiation losses are highlighted.

The electromagnetic field is expanded in terms of the complete basis of TE and TM cylindrical waves in a homogeneous reference medium; each element of the basis corresponds to a different transverse wavenumber k_{t}. The transverse features in each longitudinally invariant section of the device are accounted for by coupled-mode theory, and described with a generalized transmission matrix formalism. Appropriate boundary conditions, relating backward to forward waves at the VCSEL terminations allow to close the electromagnetic problem. The requirement for a mode to repeat itself after a full cavity round-trip defines an eigenproblem, whose solutions are related to the modal wavelengths and their corresponding threshold gains (eigenvalues) and the field expansion coefficients in the cylindrical wave basis (eigenvectors). More details about VELM can be found in [13], [14].

The simulator has been successfully applied to several VCSEL designs, *e.g.*: standard [18], non-circular/anisotropic [19], phase-coupled array [20], polarization-stable [21], high-contrast grating [22], [23], [24], [25] and spiral phase plate [26] devices, achieving good agreement with experiments and/or other simulators. This demonstrates its reliability as a computer-aided design tool.

For the structure sketched in Fig. 1, Fig. 2 reports the emission wavelength λ and the threshold gain G_{th} versus the air-gap width w_{ag}, varied in such a way to sweep a complete free spectral range (FSR). If the material gain is sufficient, the FSR coincides with the tuning range (TR).

The threshold gain features a minimum at the TR center and two maxima, twice as large, at its edges. A possible
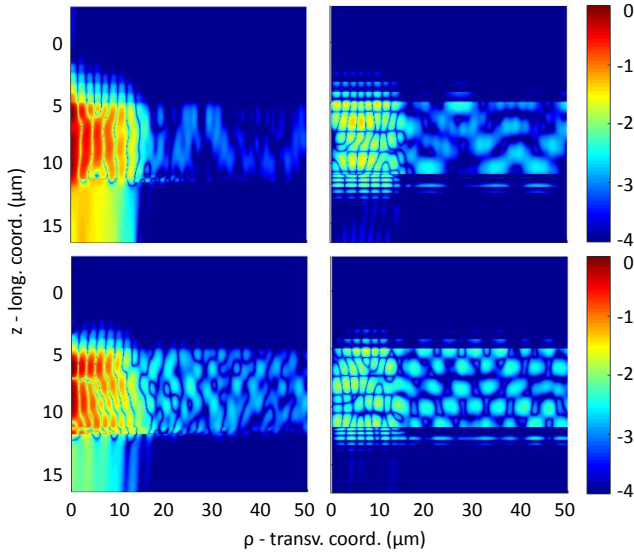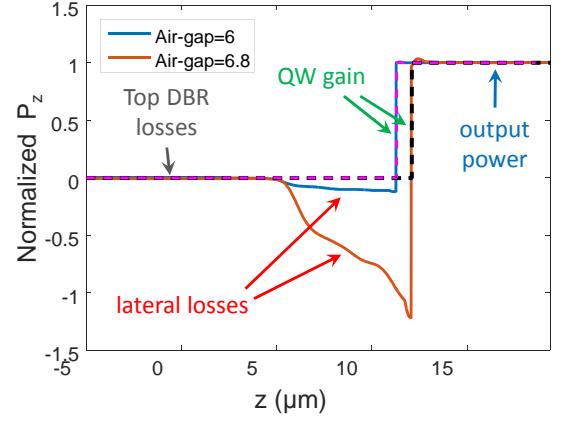

Fig. 3. Maps of the Poynting vector z (left) and ρ (right) components in the (z, x) plane, in logarithmic scale, normalized to the maximum value of the S_z component. Top and bottom maps refer to $w_{\mathrm{ag}} = 6\,\mu\mathrm{m}$ and $w_{\mathrm{ag}} = 6.8\,\mu\mathrm{m}$,
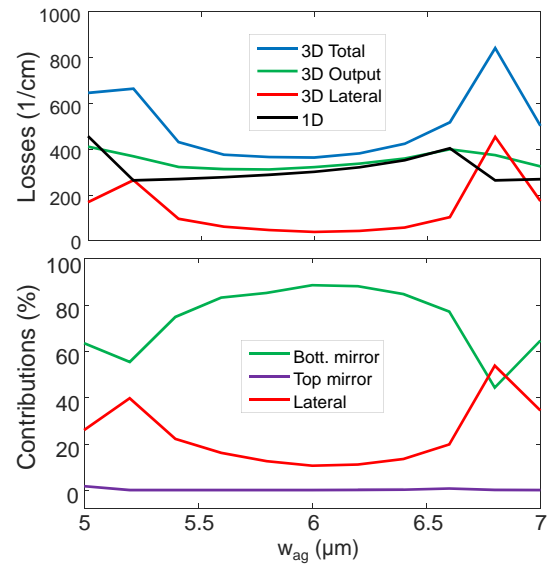

Fig. 5. Top: threshold gain (blue line, same as in Fig. 2) and its main contributions: output (bottom mirror, green line), lateral radiation (red line). The black curve refers to 1-D estimates. Bottom: corresponding percentages to the total threshold gain; the green, purple, and red curves refer to bottom mirror, top mirror and lateral losses.
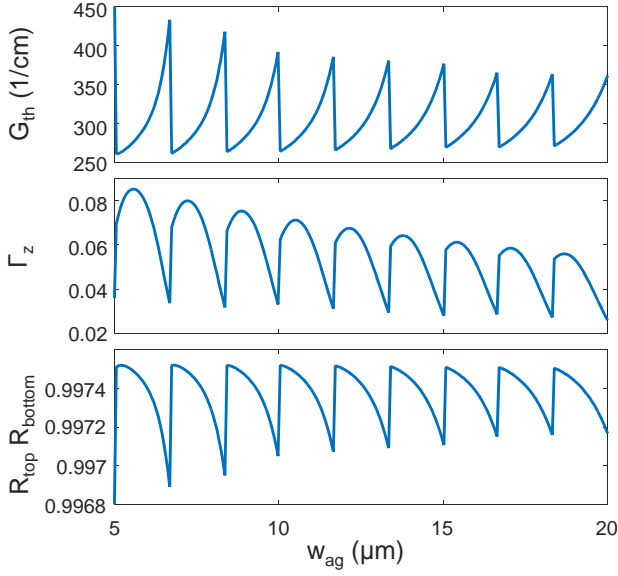
Fig. 6. 1-D simulation results. Top: threshold gain per QW. Center: confinement factor Γ_z. Bottom: product of the top and bottom DBR reflectivities seen from the inside of the cavity.

Fig. 7. Top: TE reflectivity angular spectra, expressed as number of 9 (that is, $R^{\#9} = -\log_{10}(1-|R|^2)$). Bottom: TE VELM eigenvector components, normalized with respect to the maximum value, reported in logarithmic scale. Quantities are reported versus the normalized transverse wavenumber k_t. Green and red curves refer to $w_{ag} = 6\,\mu\text{m}$ and $w_{ag} = 6.8\,\mu\text{m}$.

way to investigate such strong variation is to monitor the real part of the Poynting vector $\mathbf{S}$, which quantifies magnitude and direction of the power flux density. Hence, Fig. 3 shows the components of the Poynting vector in the (ρ, z) plane in logarithmic scale, for the two values of w_{ag} where G_{th} is minimum and maximum. In both cases the Poynting vector has a non-negligible ρ component, showing that an appreciable amount of power escapes from the sides of the device (see also Fig. 10). A synthetic representation of lateral radiation losses is obtained by defining the longitudinal power P_z as the integral of the z component of the Poynting vector on the transverse VCSEL section:

$$P_z(z) = \int \mathbf{S} \cdot \hat{\mathbf{z}} \, \rho \, \mathrm{d}\rho \, \mathrm{d}\varphi. \tag{1}$$

Figure 4 reports P_z normalized to its output value, at each longitudinal section z, for two air-gaps. The 1-D simulation (also provided as a reference) cannot account for any transverse feature, therefore the power profiles in such absorption-free VCSEL are constant except in the active region, which compensates for the radiation losses. The active region can be seen as a "lumped" source that produces a power step discontinuity. The most striking difference between 1-D and 3-D simulations is the power drop in the air-gap region. This phenomenon, which increases the power that the quantum wells (QWs) must provide in order to achieve self-consistency, is caused by the lateral radiation losses shown in Fig. 3. As a matter of fact, the jump in the red curve is almost twofold larger than in the blue curve, which corresponds to a proportional increase in the total threshold.

To validate our approach, we verified that the radiated optical power in the radial direction (flux integral of S_ρ over cylinders of increasing radii) changes continuously within the active region and then remains constant out of it.
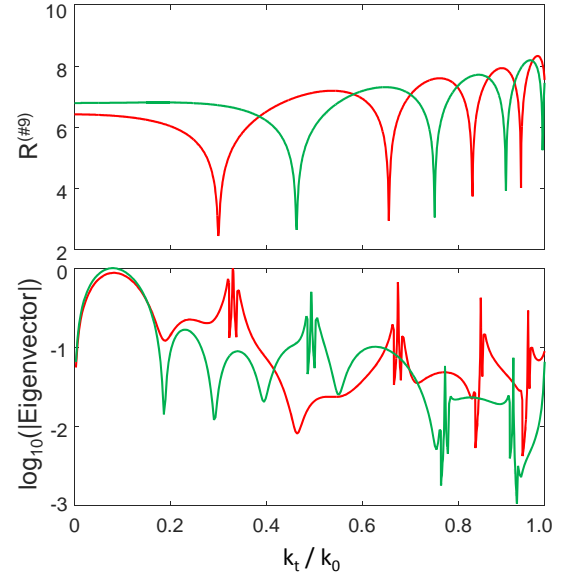
The Poynting vector analysis allows to distinguish three different radiation losses:

- top mirror (almost negligible),
- lateral radiation,
- bottom mirror (output power).

The last item allows to define the optical efficiency as the ratio of the bottom mirror output to the total losses. Similarly, one can define the lateral and top relative losses. These three contributions are reported in Fig. 5 versus the air-gap width. Threshold gain variations in the transition between two FSRs can be also observed in 1-D simulations and are related to the switch between two longitudinal modes. In such situations a misalignment between standing wave maxima and QW occurs. As a consequence, the longitudinal confinement factor defined as

$$\Gamma_z = \frac{\displaystyle\int_{\text{QW}} n^2(z) \, |E(z)|^2 \, \mathrm{d}z}{\displaystyle\int_{\text{VCSEL}} n^2(z) \, |E(z)|^2 \, \mathrm{d}z} \tag{2}$$

displays minima (see Fig. 6, center), which are related to the maxima of the threshold gain (see Fig. 6, top). In fact, the threshold gain is related to the material gain by: $G_{th} = \Gamma_z G_{QW}$. Moreover, the confinement factor decreases for increasing w_{ag}, since the field spreads over longer air-gaps while remaining almost unchanged in the active region. The bottom plot reports the product of the top and bottom DBR reflectivities seen from the inside of the cavity. Notice that this is a function of w_{ag}, which controls the oscillation frequency. These results suggest that the spectral alignment of the DBRs and the resonator is not perfect. However, 3-D effects (see Fig. 5) recover the desired symmetric behavior, but

Fig. 9. (ρ, z) refractive index color maps for the "ring of loss" toy device. The relevant details are magnified.
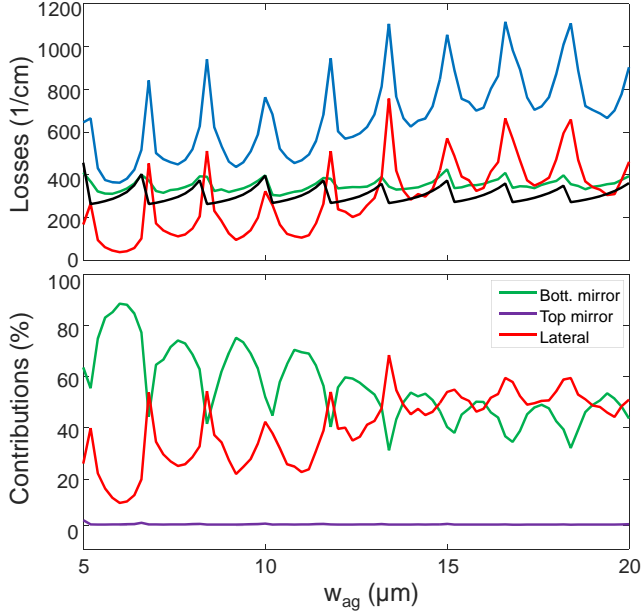
Fig. 8. Top: threshold gain (blue line, same as in Fig. 2) and its main contributions: output (bottom mirror, green line), lateral radiation (red line). The black curve refers to 1-D estimates. Bottom: corresponding percentages to the total threshold gain; the green, purple, and red curves refer to bottom mirror, top mirror and lateral losses.

the corresponding peaks are much higher than in the 1-D case, owing to the presence of lateral radiation losses.

III. UNDERSTANDING LATERAL RADIATION LOSSES

In order to gain a better understanding of the phenomenon that causes such lateral radiation losses, in Fig. 7 (bottom) we show the VELM TE eigenvector elements versus the transverse wavenumber k_t (normalized to $k_0 = 2\pi/\lambda$), for the two air-gaps analyzed in Figs. 3, 4 and consequently for the two corresponding oscillation frequencies. TM components are not reported, since they have similar behavior. Waves with $k_t > k_0$ are not included in the simulations because evanescent in the air-gap and then not contributing to the oscillation mode representation. Even on such a large k_t interval, no decay can be observed in the eigenvector elements, which instead feature particularly large values at certain k_t. This behavior is strange and strongly differs from that of a standard monolithic VCSEL, where the elements always show a fast decay and become negligible above a k_t value of the order of $0.2k_0$. To investigate this phenomenon, in Fig. 7 (top) we plot the reflection coefficient of the whole VCSEL stack versus k_t. As well known, the dips in the reflection spectrum identify the wavenumbers of the cylindrical waves that resonate in the cavity. The eigenvector peaks correspond to the dips in the reflection spectrum, indicating the presence of "off-normal resonating waves" in the oscillating mode. By observing that the strongest losses are associated with the mode whose eigenvector has the highest peaks (red curve), we can infer that those "off-normal" components are responsible for the remarkable radial component of the Poynting vector.

Long cavities have been demonstrated beneficial for single transverse mode operation by the Ulm University group [27].
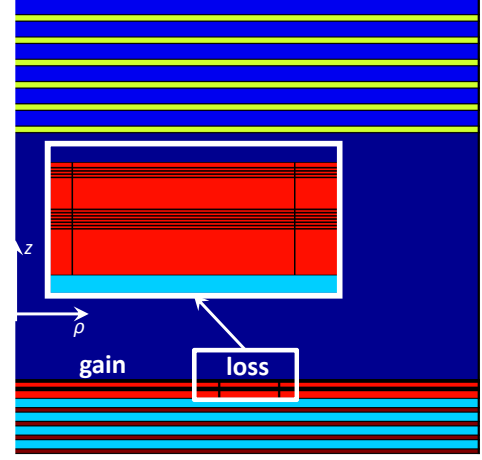
However, this introduces a penalty on the fundamental mode threshold gain, which increases with the cavity length. This is consistent with the results of Fig. 8, where the lasing features presented in Fig. 5 are reported for an extended air-gap range. In fact, from the bottom plot it can be noted that the lateral optical losses grow with the air-gap size. They become dominant for $w_{ag} > 12\,\mu$m, to the detriment of the output power. The corresponding higher threshold gain, which can be noticed in the top figure, can be easily explained by the number of "off-normal" resonating waves, which increases with the air-gap size (see e.g. Fig. 15).

During the early investigations of oxide-confined GaAs VCSELs [16], loss mechanisms were noticed and related to the presence of the oxide aperture, which provides both current and field confinement. Focusing on this second point, a finite aperture field develops a curved wavefront when propagating. This effect can generate optical leakages, which in the VCSEL community are commonly referred to as *diffraction* or *scattering losses*. Such losses are related to the mismatch between wavefront and mirror shapes. However, these phenomena are not harmful at all in standard oxide-aperture GaAs-based VCSELs. In fact, in $1 - \lambda$ cavity devices this effect plays almost no role. Thermal lensing phenomena, which increase with pumping, mostly compensate for diffraction losses in III-V VCSELs as well as lens-tapered oxide aperture profiles, which are a natural consequence of the AlAs oxidation process [28].

On the other hand, scattering losses must be carefully taken into account when the cavity length becomes large. This is the case of most tunable devices that require an air-gap as tuning mechanism such as microcavities [29], [30] or VCSELs [12].

One could be tempted to relate scattering losses in VCSELs also to sharp dielectric corners in the cavity, featured by both the oxide aperture and/or the mesa. To prove that this is not the case, the completely flat geometry shown in Fig. 9 is investigated. The active region consists of multiple QWs, which are pumped only in their central part $\rho < 10\,\mu$m. In the ring $10\,\mu$m$< \rho <13\,\mu$m QWs are unexcited, and we assume in this region $3500\,$cm^{-1} absorption loss; the real part of the
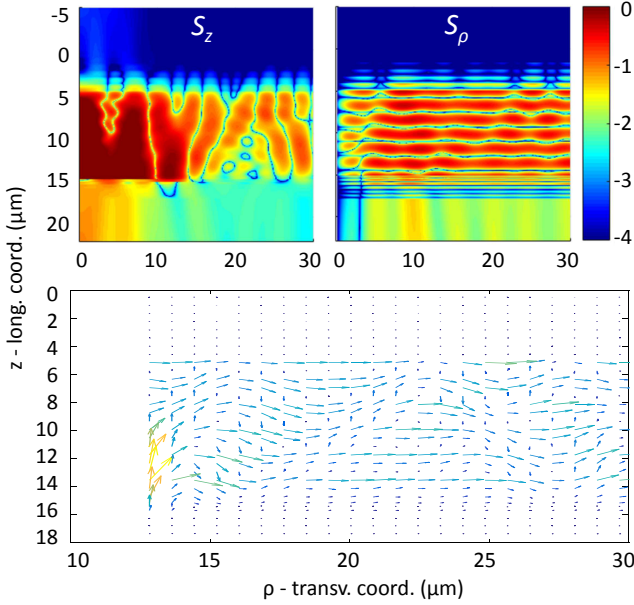
Fig. 10. Top: maps of the Poynting vector z (left) and ρ (right) components in the (ρ, z) plane, for $w_{\text{ag}} = 10.2\,\mu$m in logarithmic scale; both maps are normalized to the maximum value of S_z. Bottom: corresponding vector field representation in a reduced range.

refractive index is unchanged. For $\rho > 13\,\mu$m the structure is assumed lossless.

Figure 10 shows extremely strong lateral radiation losses in the air-gap. This is clear from both the intensity maps of S_z and S_ρ (top figure) and the corresponding vector field representation (bottom figure), where the outgoing lateral power flux can be appreciated. This proves that such radiation losses are not related to the presence of abrupt dielectric transverse profiles, but simply to a badly designed resonator where the flat mirrors do not match the curved phase front of the cavity field. This information is summarized in Fig. 11, where the different loss mechanisms have been highlighted, as in Fig. 4. The only difference is the presence of the two peaks related to the ring losses, which are introduced as mode-confining mechanism.

IV. MASTERING LATERAL RADIATION LOSSES

The previous simulations related the high losses with diffraction occurring in the air-gap. It is worth pointing out that etching the active material to define a mesa may also generate strong non-radiative surface carrier recombinations, which could result in additional electrical losses. For this reason, the solutions that will be proposed in the following sections will leave the active material untouched, counteracting at the same time the inherent antiguiding temperature features of lead chalcogenides. Lateral radiation losses can be tackled by introducing one or more curved optical elements in the resonator, so as to match the mode phase front shape. These strategies will be discussed in the following sections, and the corresponding results summarized and compared in Sect. IV-D.
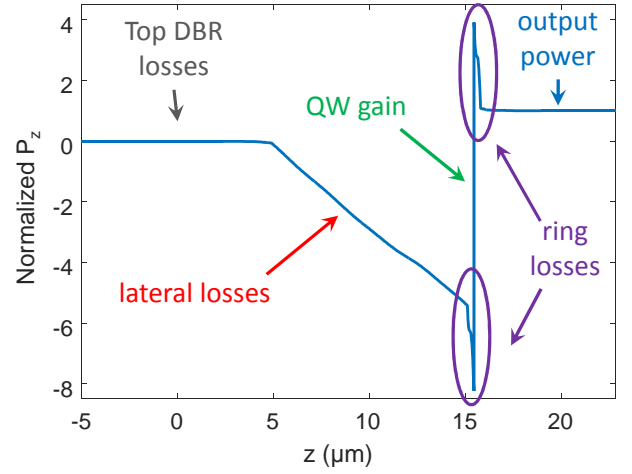

Fig. 11. Longitudinal power flux $P_z(z)$ computed according to (1) for the structure of Fig. 9. The contributions of each loss mechanism is indicated.

A. Phase front matching by curved top mirrors

The first investigated solution exploits a curved top mirror [4], [17]. A sketch of the VCSEL featuring a curved mirror with $R = 2$ mm (corresponding to $w_{\text{ag}} = 20\,\mu$m) is reported in Fig. 12 (left). This can be achieved, for example, by milling the silicon substrate on which the Si/SiO$_2$ top mirror layers are grown. An estimate of its radius of curvature can be obtained by approximating the VCSEL mode with a Gaussian beam having its waist at the active region, and recalling the expression of its radius of curvature

$$R(z) = w_{\text{ag}}\left[1 + \left(\frac{z_{\text{R}}}{w_{\text{ag}}}\right)^2\right], \qquad (3)$$

where $z_{\text{R}} = \pi w_0^2/\lambda$ is the Rayleigh range and the beam propagation distance is assumed coincident with the air-gap w_{ag}. Obviously, in a tunable VCSEL, w_{ag} is not constant. The effect of lateral radiation losses is much more relevant for long air-gaps, as it is clearly shown in Fig. 8 for the mesa VCSEL, where for $w_{\text{ag}} > 12\,\mu$m at least half of the power is always radiated in the lateral direction. Indeed, while the actual mode phase front gets increasingly curved with w_{ag} (or, from another perspective, the number of longitudinal modes grows), it remains almost flat for short air-gaps as indicated by (3).

B. Cavity-lensed approach

Although the curved mirror solution leads to an enhanced optical performance, it might be technologically demanding. For this reason, a different approach could be the insertion of a micro-lens on the active region as a constituent part of the resonator. The resulting device is sketched in Fig. 12 (right), where a lens refractive index $n = 2$ and $48\,\mu$m diameter have been assumed. This can be realized by consolidated fabrication techniques such as reflow processes [3], [31], [32]. Compared to the top curved mirror approach, additional benefits are expected from this strategy because the focusing element is closer to the active region where the field intensity is maximum and then its influence stronger. A parametric study proved that
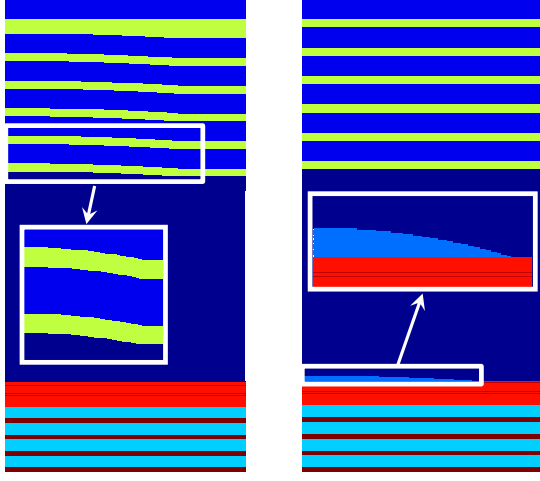
Fig. 12. (ρ, z) refractive index color maps of the VCSELs featuring a curved top mirror (left) a dielectric lens lying on the bottom active region (right). The relevant details are magnified.

good tuning performance can be obtained with a 2 mm radius of curvature as for the previous curved mirror.

C. Diffractive optical element lens

The third proposed solution is an alternative implementation of the lens concept based on a diffractive optical element (DOE), *i.e.* a Fresnel lens emulating the spherical element [33, Ch. 15]. Such component can be realized by growing a material layer on the active region and then selectively etching part of it; the circular grooves widths are modulated to follow the classical lens average index. This implementation, whose radial section is sketched in Fig. 13, consists of 19 dielectric rings, 100 nm high and spaced by 450 nm, whose smallest element is 60 nm wide, resulting in a reasonable aspect ratio. Such an approach may be particularly effective in mid-IR applications, where the polymers commonly adopted to manufacture a lens may exhibit relevant absorption losses.
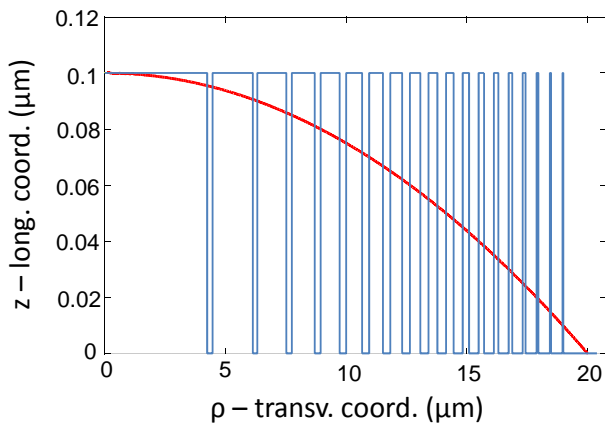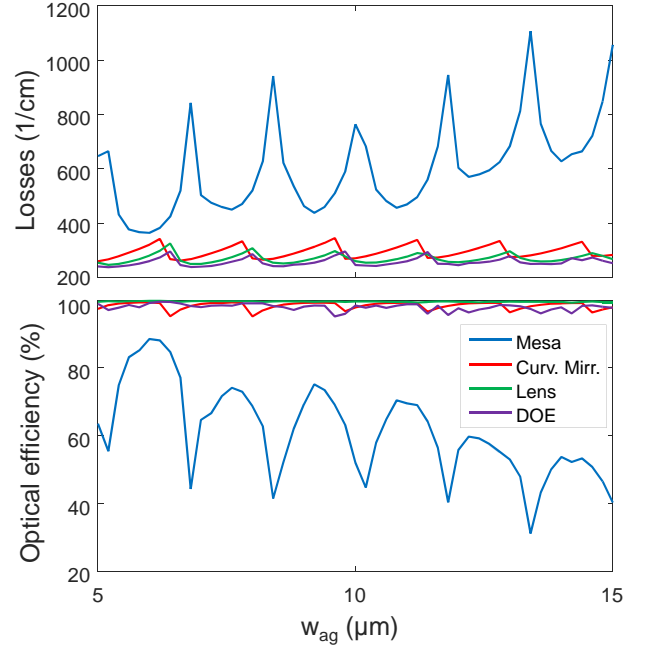

Fig. 14. Performance comparison of the proposed tunable VCSEL designs. Top: threshold gain; bottom: VCSEL optical efficiency.

D. Performance comparison

Figure 14 summarizes the performance obtained with the different designs; the top and bottom figures report the total threshold gain curves, and the VCSEL overall efficiency for the different approaches. The mesa design has the highest threshold gain and the lowest efficiency by far. In the investigated air-gap interval, the threshold gain covers the range $[400 \div 1100]\,\mathrm{cm}^{-1}$, while the proposed design reduces it to $[250 \div 350]\,\mathrm{cm}^{-1}$.

Among the three remaining solutions, the curved mirror is the less effective. The classical and DOE lens implementations exhibit very good performance under both the threshold and efficiency points of view. Figure 15 reports the VELM eigenvectors for the classical lens (blue) and for the DOE (red) with

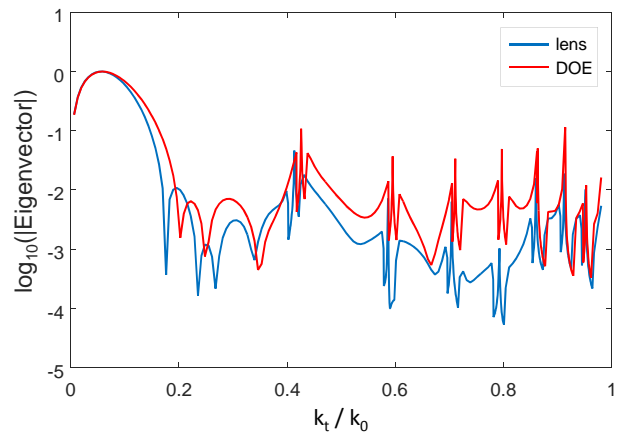Fig. 13. Radial cut of the lens (red curve) and of the approximating DOE (blue curve).

Fig. 15. TE VELM eigenvector components (reported in logarithmic scale) versus transverse wavenumber of the classical (blue) and DOE (red) lens implementations.
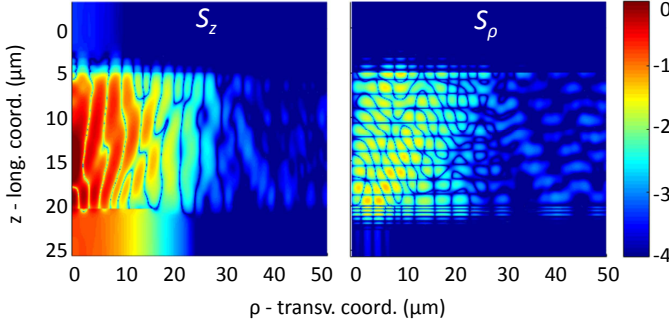
Fig. 16. Maps of the Poynting vector z (left) and ρ (right) components in the (z, x) plane, in logarithmic scale, normalized to the maximum value of the S_z component. Top and bottom maps refer to $w_{\mathrm{ag}} = 15\,\mu$m.

$w_{\mathrm{ag}} = 15\,\mu$m and allows to compare in a different manner the two designs. The portion of the eigenvector related to lateral radiation losses ($k_{\mathrm{t}} > 0.4\,k_0$) is lower for the lens design. This is reasonable, since DOE is only an approximation of a standard lens. Compared to Fig. 7 (bottom), many more peaks can be noticed, since the air-gap in this situation is much longer and then the structure supports more longitudinal modes. However, their contributions is negligible compared to the mesa case. Figure 16 shows the corresponding map of the Poynting vector for the VCSEL equipped with the DOE. As it can be seen almost no lateral radiation loss is present, being S_ρ three orders of magnitude lower than S_z out of the active region.

V. Conclusions

This paper presents a comprehensive investigation of the optical loss mechanisms affecting the tunable VCSELs threshold gain. The lateral radiation losses have been characterized by a novel approach based on the study of the Poynting vector of the simulated VCSEL mode, provided by the full-wave 3-D vector simulator VELM. The physical meaning of VELM eigenvectors allowed to obtain deeper insight into this mechanism and to recognize its connection to the well-known concept of scattering losses. This is a major advantage of our approach compared to fully-numerical techniques such as finite-difference time-domain or finite element methods. The effectiveness of three technologically-affordable solutions to these optical leakages has been proved through extensive simulation campaigns.

Acknowledgment

References

[1] R. Michalzik, Ed., *VCSELs: Fundamentals, Technology and Applications of Vertical-Cavity Surface-Emitting Lasers*. Berlin: Springer-Verlag, 2013.
[2] M. C. Y. Huang, K. B. Cheng, Y. Zhou, A. P. Pisano, and C. J. Chang-Hasnain, "Monolithic integrated piezoelectric MEMS-tunable VCSEL," *IEEE J. Select. Topics Quantum Electron.*, vol. 13, no. 2, pp. 374–380, 2007.
[3] B. Kögel, P. Debernardi, P. Westbergh, J. S. Gustavsson, A. Haglund, E. Haglund, J. Bengtsson, and A. Larsson, "Integrated MEMS-tunable VCSELs using a self-aligned reflow process," *IEEE J. Quantum Electron.*, vol. 48, no. 2, pp. 144–152, 2012.
[4] C. Gierl, T. Gruendl, P. Debernardi, K. Zogal, C. Grasse, H. A. Davani, G. Böhm, S. Jatta, F. Küppers, P. Meißner, and M.-C. Amann, "Surface micromachined tunable 1.55 μm-VCSEL with 102 nm continuous single-mode tuning," *Opt. Express*, vol. 19, no. 18, pp. 17 336–17 343, Aug. 2011.
[5] T. Klein and R. Huber, "High-speed OCT light sources and systems," *Biomed. Opt. Express*, vol. 8, no. 2, pp. 828–859, 2017.
[6] T. Ansbaek, I.-S. Chung, E. S. Semenova, O. Hansen, and K. Yvind, "Resonant MEMS tunable VCSEL," *IEEE J. Select. Topics Quantum Electron.*, vol. 19, no. 4, pp. 1 702 306–1 702 306–6, 2013.
[7] D. D. John, C. B. Burgner, B. Potsaid, M. E. Robertson, B. K. Lee, W. J. Choi, A. E. Cable, J. G. Fujimoto, and V. Jayaraman, "Wideband electrically pumped 1050-nm MEMS-tunable VCSEL for ophtalmic imaging," *J. Lightwave Technol.*, vol. 33, no. 16, pp. 3461–3468, 2015.
[8] V. Jarayaman, G. D. Cole, M. Robertson, A. Uddin, and A. Cable, "High-sweep-rate 1310 nm MEMS-VCSEL with 150 nm continuous tuning range," *Electron. Lett.*, vol. 48, no. 14, pp. 867–869, 2012.
[9] W. W. Bewley, C. L. Canedy, C. S. Kim, C. D. Merritt, M. V. Warren, I. Vurgaftman, J. R. Meyer, and M. Kim, "Room-temperature mid-infrared interband cascade vertical-cavity surface-emitting lasers," *Appl. Phys. Lett.*, vol. 109, pp. 151 108–1–151 108–5, 2016.
[10] G. K. Veerabathran, S. Sprengel, A. Andrejew, and M.-C. Amann, "Room-temperature vertical-cavity surface-emitting lasers at 4 μm with GaSb-based type-II quantum wells," *Appl. Phys. Lett.*, vol. 110, pp. 071 104–1–5, 2017.
[11] M. Fill, P. Debernardi, F. Felder, and H. Zogg, "Lead-chalcogenide mid-infrared vertical external cavity surface emitting lasers with improved threshold: Theory and experiment," *Appl. Phys. Lett.*, vol. 103, pp. 201 120–1–201 120–3, 2013.
[12] C. J. Chang-Hasnain and W. Yang, "High-contrast gratings for integrated optoelectronics," *Adv. Opt. Photonics*, vol. 4, no. 3, pp. 379–440, 2012.
[13] G. P. Bava, P. Debernardi, and L. Fratta, "Three-dimensional model for vectorial fields in vertical-cavity surface-emitting lasers," *Phys. Rev. A*, vol. 63, no. 2, pp. 23 816–1–23 816–13, 2001.
[14] P. Debernardi and G. P. Bava, "Coupled mode theory: a powerful tool for analyzing complex VCSELs and designing advanced devices features," *IEEE J. Select. Topics Quantum Electron.*, vol. 9, no. 3, pp. 905–917, 2003.
[15] A. G. Fox and T. Li, "Resonant modes in a maser interferometer," *Bell Syst. Tech. J.*, vol. 40, no. 2, pp. 453–488, 1961.
[16] E. R. Hegblom, D. I. Babic, B. J. Thibeault, and L. A. Coldren, "Scattering losses from dielectric apertures in vertical-cavity lasers," *IEEE J. Select. Topics Quantum Electron.*, vol. 3, no. 2, pp. 379–389, 1997.
[17] P. Debernardi, B. Kögel, K. Zogal, P. Meissner, M. Maute, M. Ortsiefer, G. Bohm, and M.-C. Amann, "Modal properties of long-wavelength tunable MEMS-VCSELs with curved mirrors: comparison of experiment and modeling," *IEEE J. Quantum Electron.*, vol. 44, no. 4, pp. 391–399, 2008.
[18] P. Bienstman, R. Baets, J. Vukusic, A. Larsson, M. J. Noble, M. Brunner, K. Gulden, P. Debernardi, L. Fratta, G. P. Bava, H. Wenzel, B. Klein, O. Conradi, R. Pregla, S. A. Riyopoulos, J.-F. P. Seurin, and S. L. Chuang, "Comparison of optical VCSEL models on the simulation of oxide-confined devices," *IEEE J. Quantum Electron.*, vol. 37, no. 12, pp. 1618–1631, 2001.
[19] P. Debernardi, G. P. Bava, C. Degen, I. Fischer, and W. Elsäßer, "Influence of anisotropies on transverse modes in oxide-confined VCSELs," *IEEE J. Quantum Electron.*, vol. 38, no. 1, pp. 73–84, 2002.
[20] P. Debernardi, G. P. Bava, F. Monti di Sopra, and M. B. Willemsen, "Features of vectorial modes in phase-coupled VCSEL arrays: experiments and theory," *IEEE J. Quantum Electron.*, vol. 39, no. 1, pp. 109–119, 2003.
[21] P. Debernardi, J. M. Ostermann, M. Sondermann, T. Ackermann, G. P. Bava, and R. Michalzik, "Theoretical-experimental study of the vectorial modal properties of polarization-stable multimode grating VCSELs," *IEEE J. Select. Topics Quantum Electron.*, vol. 13, no. 5, pp. 1340–1348, 2007.
[22] P. Debernardi, R. Orta, T. Gründl, and M.-C. Amann, "3-D vectorial optical model for high-contrast grating vertical-cavity surface-emitting lasers," *IEEE J. Quantum Electron.*, vol. 49, no. 2, pp. 137–145, 2013.
[23] A. Tibaldi, P. Debernardi, and R. Orta, "High-contrast grating performance issues in tunable VCSELs," *IEEE J. Quantum Electron.*, vol. 51, no. 12, p. 2400407, 2015.

[24] R. Orta, A. Tibaldi, and P. Debernardi, "Bimodal resonance phenomena–Part I: generalized Fabry–Pérot interferometers," *IEEE J. Quantum Electron.*, vol. 52, no. 12, pp. 6 100 508–1–6 100 508–8, 2016.

[25] A. Tibaldi, P. Debernardi, and R. Orta, "Bimodal resonance phenomena–Part III: high-contrast grating reflectors," *IEEE J. Quantum Electron.*, vol. 54, no. 6, pp. 6 600 108–1–6 600 108–8, 2018.

[26] P. Debernardi, A. Tibaldi, P. Gerlach, P. Martelli, P. Boffi, M. Martinelli, D. Coviello, and R. Orta, "Modal performance of spiral phase plate VCSELs," *IEEE J. Quantum Electron.*, vol. 52, no. 5, pp. 2 400 108–1–2 400 108–8, 2016.

[27] H. J. Unold, S. W. Z. Mahmoud, R. Jäger, M. Kicherer, M. C. Riedl, and K. J. Ebeling, "Improving single-mode VCSEL performance by introducing a long monolithic cavity," *IEEE Photon. Technol. Lett.*, vol. 12, no. 8, pp. 939–941, 2000.

[28] L. A. Coldren, B. J. Thibeault, E. R. Hegblom, G. B. Thompson, and J. W. Scott, "Dielectric apertures as intracavity lenses in verticalcavity lasers," *Appl. Phys. Lett.*, vol. 68, no. 3, pp. 313–315, 1996.

[29] J. Peerlings, A. Dehé, A. Vogt, M. Tilsch, C. Hebeler, F. Langenhan, P. Meissner, and H. L. Hartnagel, "Long resonator micromachined tunable GaAs-AlAs Fabry-Pérot filter," *IEEE Photon. Technol. Lett.*, vol. 9, no. 9, pp. 1235–1237, 1997.

[30] M. Aziz, J. Pfeiffer, and P. Meissner, "Modal behaviour of passive, stable microcavities," *Phys. Status Solidi A*, vol. 188, no. 3, pp. 979–982, 2001.

[31] A. Kroner, I. Kardosh, F. Rinaldi, and R. Michalzik, "Towards VCSEL-based integrated optical traps for biomedical applications," *Electron. Lett.*, vol. 42, no. 2, pp. 93–94, 2006.

[32] C. Levallois, V. Bardinal, C. Vergnenègre, T. Leichlé, T. Camps, E. Daran, and J.-B. Doucet, "VCSEL collimation using self-aligned integrated polymer microlenses," in *Proc. SPIE 6992*, May 2008, pp. 69 920W–1–8.

[33] K. Iizuka, *Engineering optics*, 1st ed. Berlin: Springer-Verlag, 1985.

Pierluigi Debernardi was born in Casale Monferrato and received his degree in Electronics Engineering in 1987 from Politecnico di Torino, Italy. Since 1989 he's with the Italian National Council of Research at Politecnico di Torino. His interests are mainly in the field of the modeling of semiconductor materials and devices for optoelectronic applications. Recently he is mostly involved in modeling and designing VCSEL structures with non-circular and/or complex geometries, so as to achieve specific performances.

Alberto Tibaldi was born in Casale Monferrato, Italy, in 1987. In 2009, 2011 and 2015 he received the B.Sc., M.Sc. and Ph.D. degrees in Electronic Engineering from Politecnico di Torino. In 2012 he joins the Italian National Council of Research (CNR) as a research fellow. Currently he teaches courses on numerical analysis and semiconductor device simulation. His scientific interests mainly regard the electrical and optical modeling of photonic devices.

Renato Orta (M'92-SM'99) is a member of the Department of Electronics, Politecnico di Torino, since 1974. He joined the Department as Assistant Professor in 1981, in 1987 became Associate Professor and since 1999 is Full Professor. He currently teaches courses on electromagnetic field theory and optical components. His research interests include the areas of microwave and optical components, radiation and scattering of waves and numerical techniques. He is Senior Member of the IEEE.